Supporting information

Characterization of the platinum-carbon interface for electrochemical applications

Elena Willinger[1,2], Andrey Tarasov[1], Raoul Blume[1,2], Ali Rinaldi[1,4], Olaf Timpe[1], Cyriac Massué[1,2], Michael Scherzer[1,2], Johannes Noack[1], Robert Schlögl[1,2] and Marc Georg Willinger[1,2,3*]

[1]*Department of Inorganic Chemistry, Fritz-Haber-Institut der Max-Planck-Gesellschaft, Berlin (Germany)*

[2]*Max Planck Institute for Chemical Energy Conversion, Stiftstrasse 34-36, 45470 Mülheim an der Ruhr (Germany)*

[3]*Max Planck Institute of Colloids and Interfaces, Department of Colloid Chemistry, Research Campus Golm, 14424 Potsdam, (Germany)*

[4]*Chemistry Department King Fahd University of Petroleum & Minerals, Dhahran 31261 (Saudi Arabia)*

*e-mail: willinger@fhi-berlin.mpg.de

Raman

Further insight about the degree of graphitic ordering is provided by Raman spectroscopy. It is known that Raman spectra of disordered nanocarbons show a G-band peak at around 1588 cm^{-1} due to graphitic contributions, a D-band at 1350 cm^{-1} and D$^{/}$-band at *ca.* 1620 cm^{-1} attributed to a defective carbon, a D$^{//}$-band at *ca.* 1495 cm^{-1} due to amorphous carbon and finally, an I-band at *ca.* 1190 cm^{-1}, which is associated to ionic impurities.[23-25] Figure 1b shows normalized Raman spectra of the three carbon supports and for reference, one spectrum recorded from highly ordered pyrolytic graphite (HOPG). All spectra are normalized to the intensity of the G band such that different degrees of disorder are reflected in the intensity of the D-band peaks. While the D-band is barely visible in the spectrum of HOPG in figure 1b, its intensity is significantly higher for the carbons A, B and C. Moreover, a broadening of the D-band for the B and C carbons and a shift of the G-band towards higher frequencies[27] is observed, indicating a significant D$^{/}$-band contribution for the B and C carbons. To abstract information about the degree of graphitization, the 5-peak-fitting[28] procedure was applied using Lorenz functions for

the G, D, D/ and I-bands and a Gauss function for the D$^{//}$-band, respectively (Figure S1). Obtained values for the I_D/I_G ratio are listed in the Table 1. One can see that the Raman and XRD data show the same trend of decreasing graphitic ordering from A to C. The I_D/I_G ratio can further be used to estimate the in-plane crystallite size (La) of disordered carbons via the following equation:[26]

La (nm) = 2.4 x 10-10 λ_{laser}^4 I_G/I_D (S1),

where λ_{laser} is the laser wavelength of 532 nm.

The comparison of in-plane crystallite sizes with interlayer domain sizes shows the same trend of decreasing graphitic ordering from carbon A to C. In order to obtain further structural information, we now switch from integral spectroscopic and diffraction methods to real-space local imaging by transmission electron microscopy.
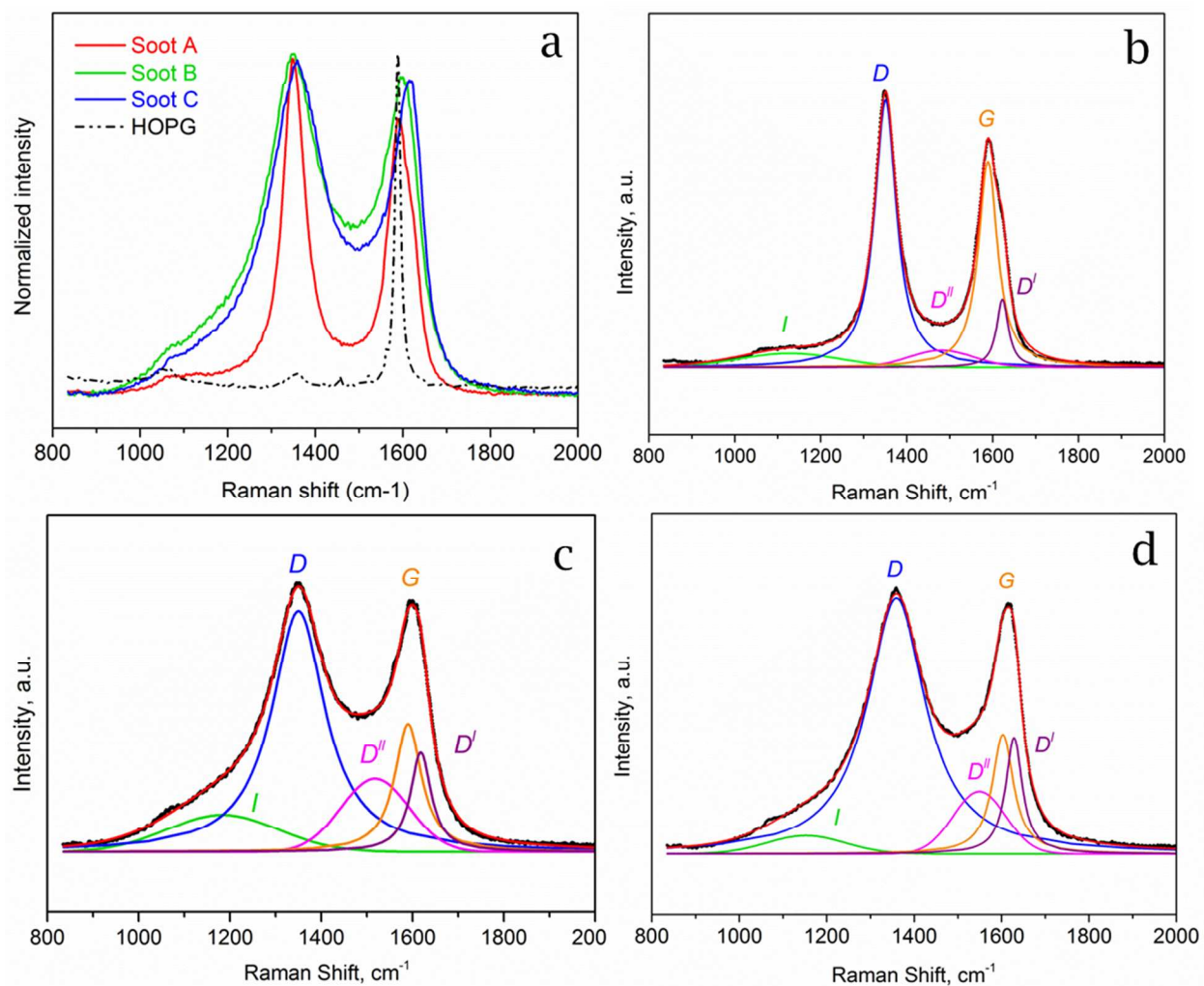
Figure S1. Raman spectroscopy results. a) Comparison of Raman spectra of HOPG (black spectrum), carbon A (red spectrum), carbon B (green spectrum) and carbon C (blue spectrum) samples; deconvoluted Raman spectra of carbon A (b), carbon B (c) and carbon C (d), respectively.
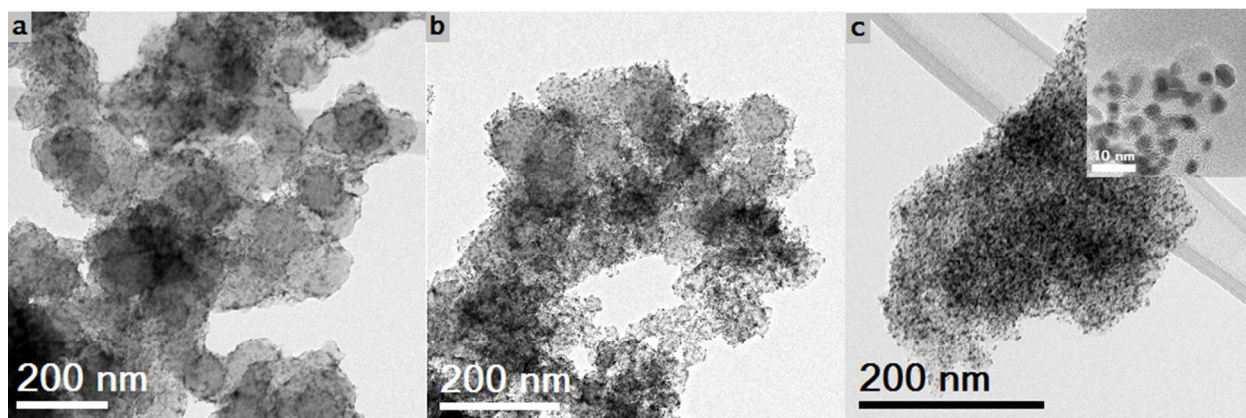
Figure S2. TEM overview images of Pt on different carbon supports: (a) Pt/carbon A with carbon particle sizes at about 100 nm; (b) Pt/carbon B with including both high surface area particles with about 20 nm diameter and low surface area particles, comparable with carbon A; (c) Pt/carbon C consists of carbon particles of about 7 nm (see the HRTEM in the top right corner).

The CSR estimated from XRD peak broadening can be directly visualized by applying the fast Fourier transform (FFT) filtering procedure on HRTEM images recorded in real space. The FFT-filtering can be considered as an analog to TEM dark-field imaging.[27] It enables the visualization of coherently scattering regions by selecting specific spatial frequencies, i.e., spots or rings in reciprocal space. (Fig. S3).
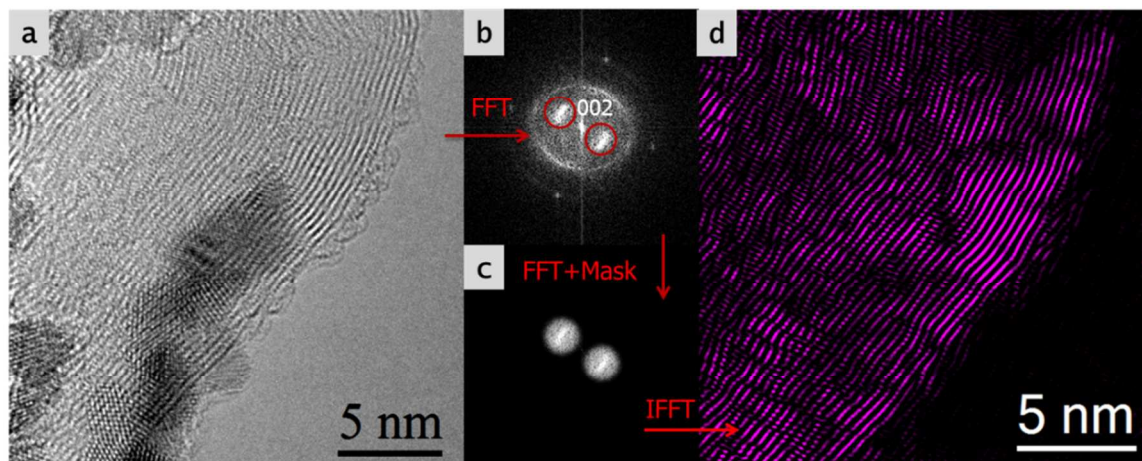

Figure S3. The CSRs can be visualized by using FFT filtering of the associated spatial frequencies in the HRTEM images. The example shows the original HRTEM image of Pt/carbon A (a) and the corresponding FFT pattern (b). To visualize coherent scattering regions contributing to the interlayer (002) diffraction maxima, a mask selecting only these intensities in

the FFT pattern is applied (c). Inverse FFT of the selected spatial frequency results in a picture that shows the regions that contain defined (002) planes (d).
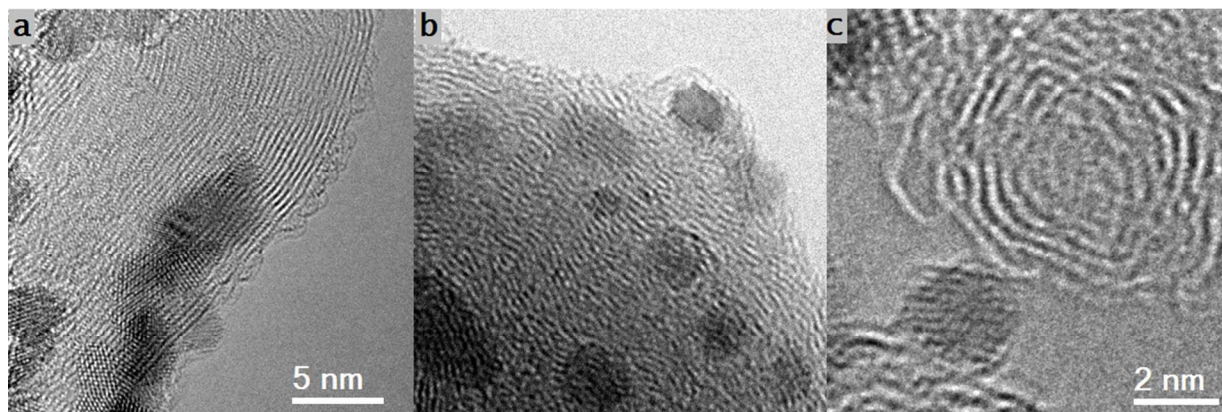

Figure S4. The original HRTEM images of carbon structures of Carbon A (a), Carbon B (b) and Carbon C (c), respectively.
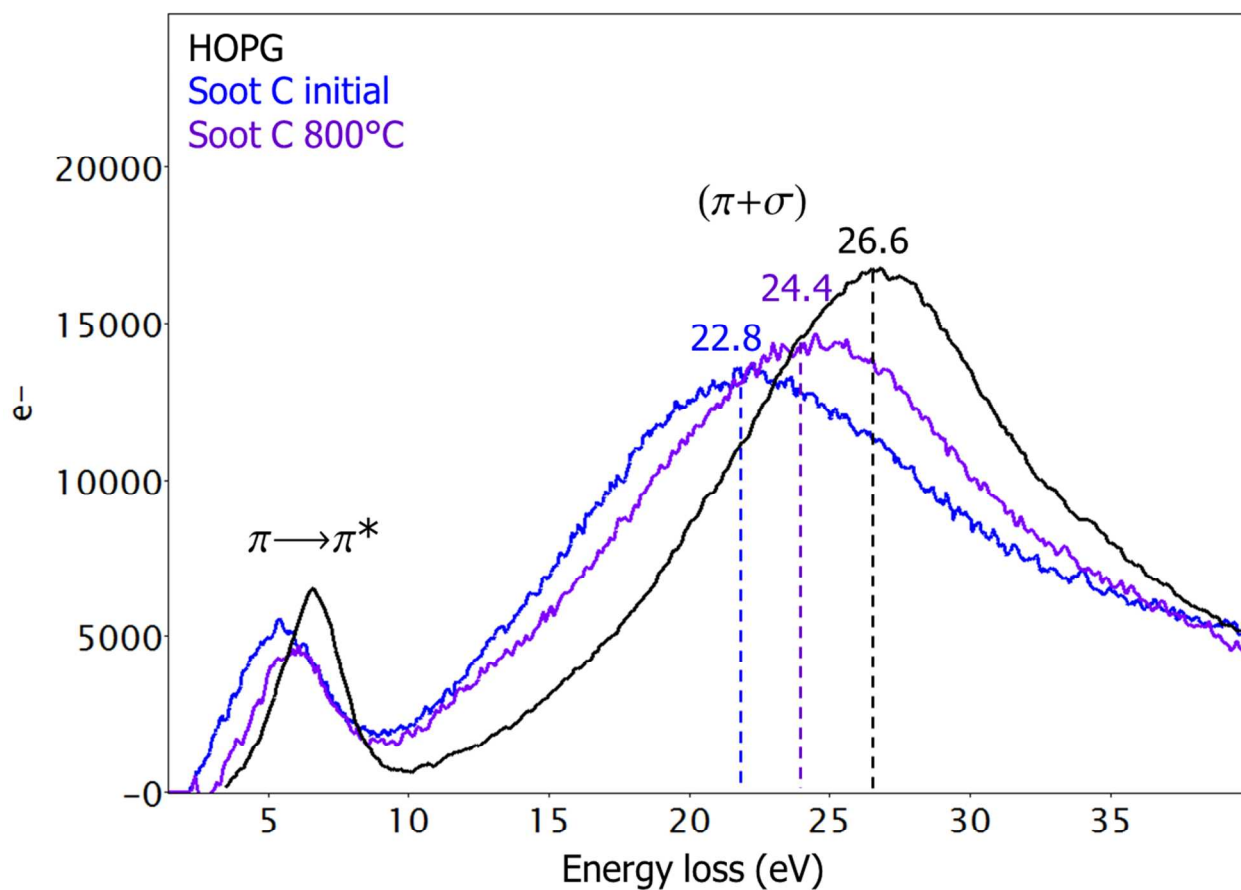
Figure S5. EELS low loss spectra of the initial state of the carbon C (blue spectrum), the annealed carbon C at 800°C in vacuum (violet spectrum) and the HOPG (black spectrum).

Table S1. A comparison between structural characteristics of Carbon B and Vulcan XC-72

Sample	DTA-TGA, T peak°C	S_{BET} m^2/g	V_{total} m^3/g	$V_{\mu icro}$ m^3/g	V_{meso} m^3/g	d_{002} Å	I_D/I_G
Vulcan XC-72[1]	648[1]	262[1]	0.32[1]	0.05[1]	0.27[1]	3.6[2]	2.14[1*]
Carbon B	630	247	1.67	0.04	1.63	3.58	2.1[*]

[1] *Yaovi Holade et al., Phys. Chem. Chem. Phys.,2014, 16, 25609*

[2] *Luis Castanheira et al.,ACS Catal. 2015, 5, 2184−2194*

[*] To compare the I_D/I_G ratio of carbon B with the literature, the Raman spectra fitting was performed with 4 bands: I, D, D$^{//}$ and G.

According to the literature studies on Vulcan XC-72, the structural properties abstracted from BET, XRD, Raman and TG indicate some similarity between carbon B and Vulcan XC-72.[1-2] However, carbon B has a much higher content of mesopores, which is reflected by a good dispersion of metal particles (Fig. S2).

Table S2. XRF analysis of pure carbon blacks.

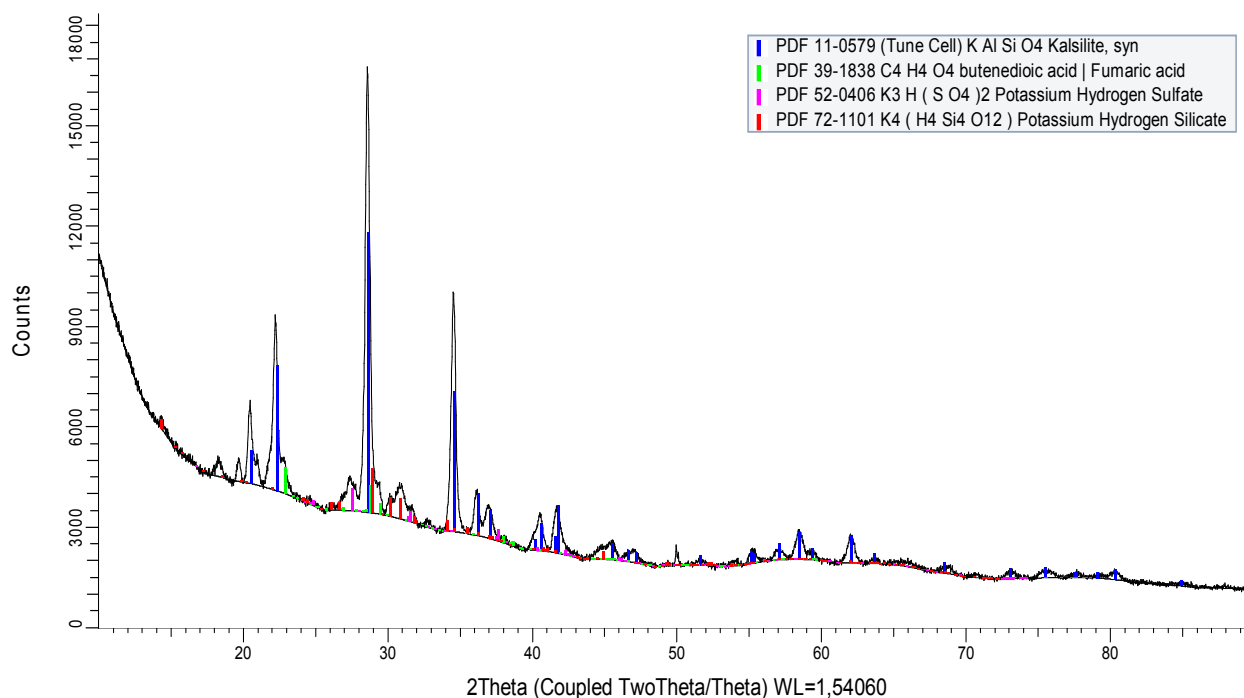| Carbon A	Concentration wt.%
C	100
Fe	0.002
Carbon B	
C	99.7
Fe	0.003
S	0.312
Ca	0.002
Carbon C	
C	99.5
Fe	0.0043
S	0.274
K	0.0859
Si	0.047
Mg	0.006
Al	0.054

Figure S6. XRD pattern of residues from carbon C collected after thermal oxidation.

Thermokinetic analysis of the initial supports

Typically 5 mg of sample were loaded in an Al_2O_3 crucible (85µl). The temperature programmed oxidation (TPO) experiments were carried out using a flow of 21% O_2 in Ar. The temperature was ramped to 1000 °C at a heating rate of 5 °C/min. Temperatures were calibrated against the melting points of In, Sn, Bi, Zn, Pb, Al and Au. For quadrupole mass spectrometry, an electron ionization energy of 60 eV and a dwell time per mass of 0.2 s were used. The main mass gates used were m/e18 (H_2O), 28 (CO), 30 (NO), 32 (O_2), 44 (CO_2), and 46 (NO_2). Prior to the experiments the mass-spectrometer was calibrated for CO_2 and CO by introducing 500µl gas pulses. The resulting peak area was used to calculate the calibration factors for quantitative analysis of the gas phase.

The kinetic data obtained in the experiments were processed using the Netzsch software. The Proteus Thermal Analysis program was used for mathematical processing of the raw TG/DSC/MS curves and to determine heats, onset temperatures of degradation and mass

changes. The integration of DSC heat effects was performed using tangential baselines. The Thermokinetics program was used for processing kinetic dependencies and for solving the direct and inverse kinetic problems. For all models under consideration, a set of statistical criteria of adequacy was used according to the Netzsch procedure.[18] The optimal model was selected on the basis of the discrepancies between the calculated and experimental values. Conversion α is defined as the fraction of the initial reagent that has reacted at time t_i and changes from 0 to 1. The conversion can be calculated from both the TG and DSC data, as well as from differential thermogravimetry DTG data. For integral measurements (thermogravimetry) the measured curve is converted to the plot of conversion versus time t_i by the formula:

$$\alpha_i = \frac{m(t_s) - m(t_i)}{m(t_s) - m(t_f)} \tag{S2}$$

where (t_s) is the signal at the starting moment of time t_s, $m(t_j)$ is the signal at the jth moment of time t_j, and $m(t_f)$ is the signal at the final moment of time t_f.

For differential measurements (DSC, DTA, mass spectrometry), the conversion is calculated by equation (S3):

$$\alpha_j = \frac{\int_{t_s}^{t_i} [S(t) - B(t)]dt}{\int_{t_s}^{t_f} [S(t) - B(t)]dt} \tag{S3}$$

where $S(t)$ is the signal at the moment of time t and $B(t)$ is the baseline at the moment of time t.
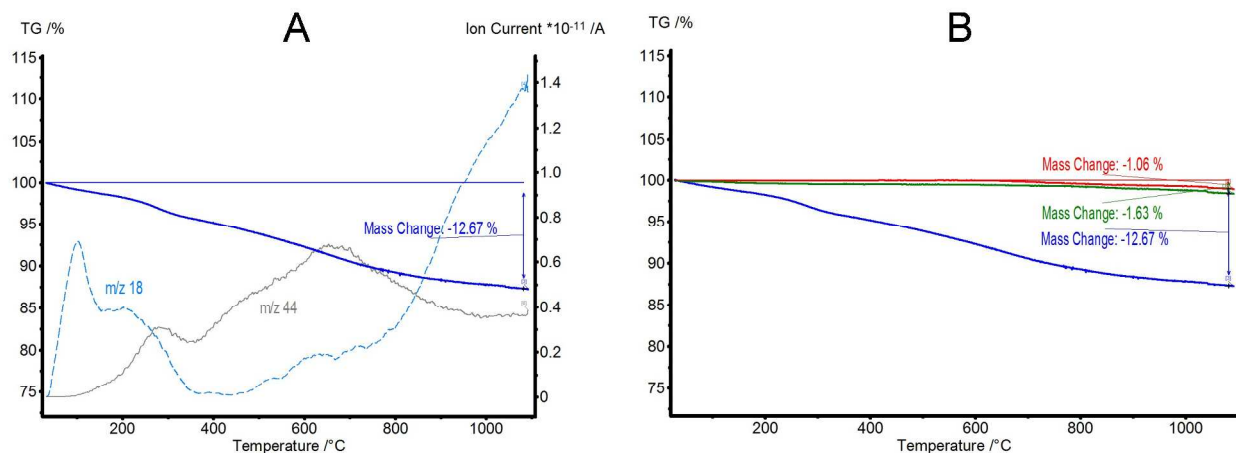
Figure S7 Temperature programmed desorption in Ar with 5 K/min. Carbon C shows the highest weight loss, which is attributed to water desorption, decomposition of hydroxy species in the high temperature range and CO_2 evolution as a product of degradation of carboxyl groups. Minor weight change is detected for carbon A and B.
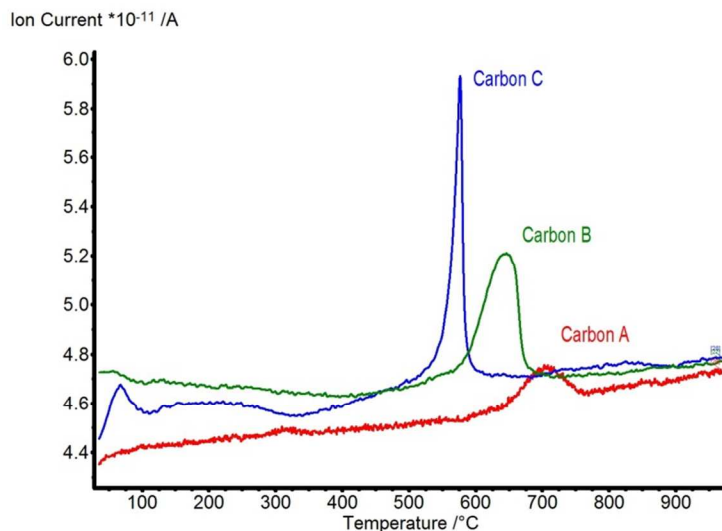

Figure S8. Ion currents of m/z 18, H_2O^+, during the oxidation of carbons at 2 K/min without background subtraction. Carbon C and B have more hydrogen contaning groups. Carbon C shows desorption of water in the low temprature range.
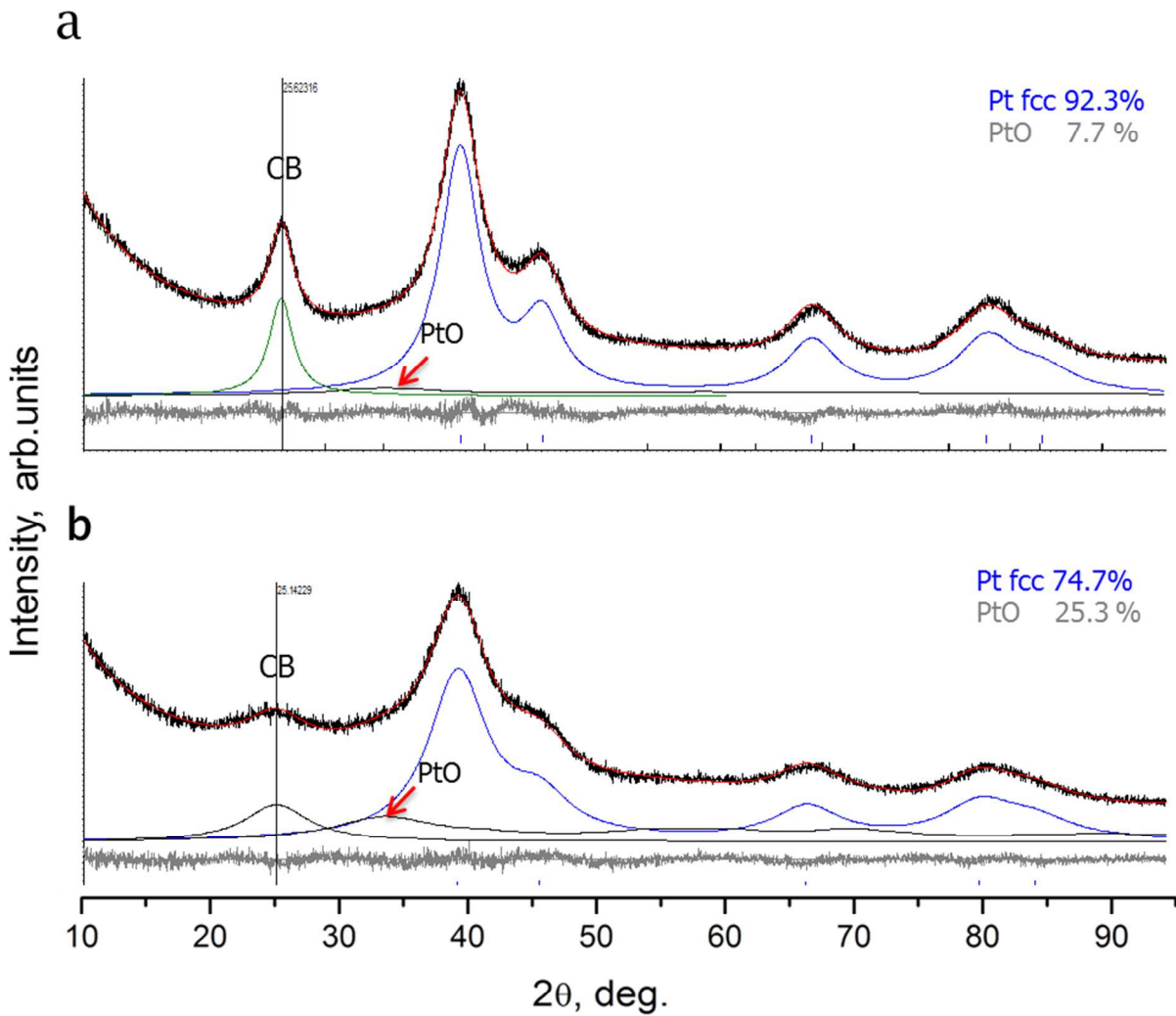
Figure S9. XRD phase composition analysis. a) Pt/carbon A shows the composition of Pt fcc 92.3% (blue pattern) and 7.7% of PtO phase (grey pattern), which appears as a broad shoulder of the (111) Pt reflection at the low Bragg angle side; b) Pt/carbon C shows the presence of higher PtO concentration in the sample (about 25%). No XRD-based phase composition analysis was performed for sample Pt/carbon B due to its very disordered and ill-defined Pt structure, which gives rise to an amorphous-like diffraction pattern.

XPS analysis of survey, C 1s and O 1s spectra

Additional information about the chemical composition of the surface of the different carbons is provided by the survey XPS data shown in Figure S10.
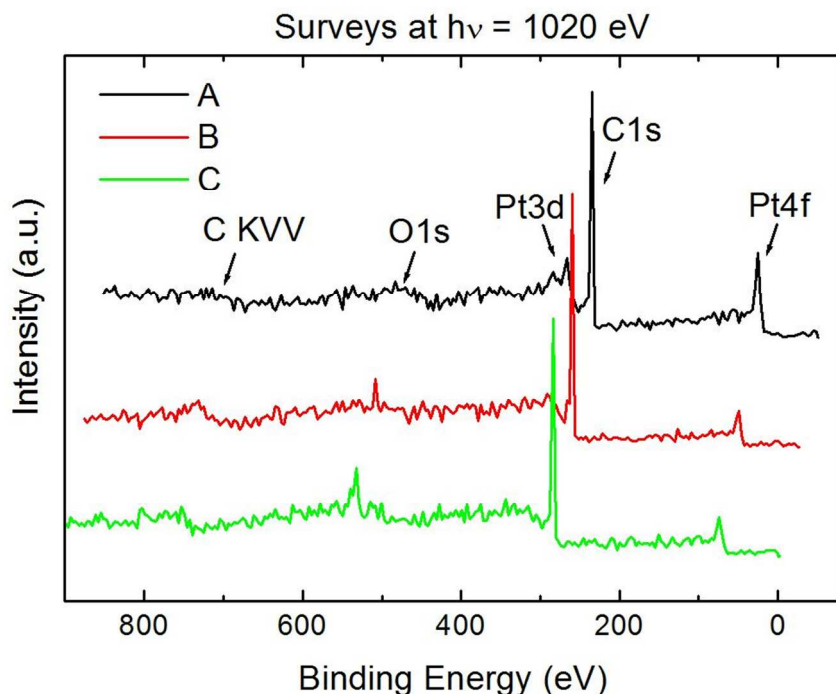

Figure S10. Waterfall plot showing XPS survey spectra of Pt/carbon A (black), Pt/carbon B (red) and Pt/carbon C (green), respectively.

In order to provide more information about the character of functional groups at the surface of the carbons, additional analysis of the O 1s XPS recorded before and after annealing was performed. The O 1s XPS data in Figure S11 shows a higher amount of oxygen on carbon B and C compared to carbon A. A large portion of the oxygen is due to Pt oxides and –hydroxides, which is confirmed by the drop in the associated intensity upon annealing at 100 °C. The C-O bonds, on the other hand, remain unchanged, as can be seen in the corresponding C 1s XPS spectra. Overall, carbon B has slightly more oxygen in the surface than carbon C, and both contain a lot more than carbon A.
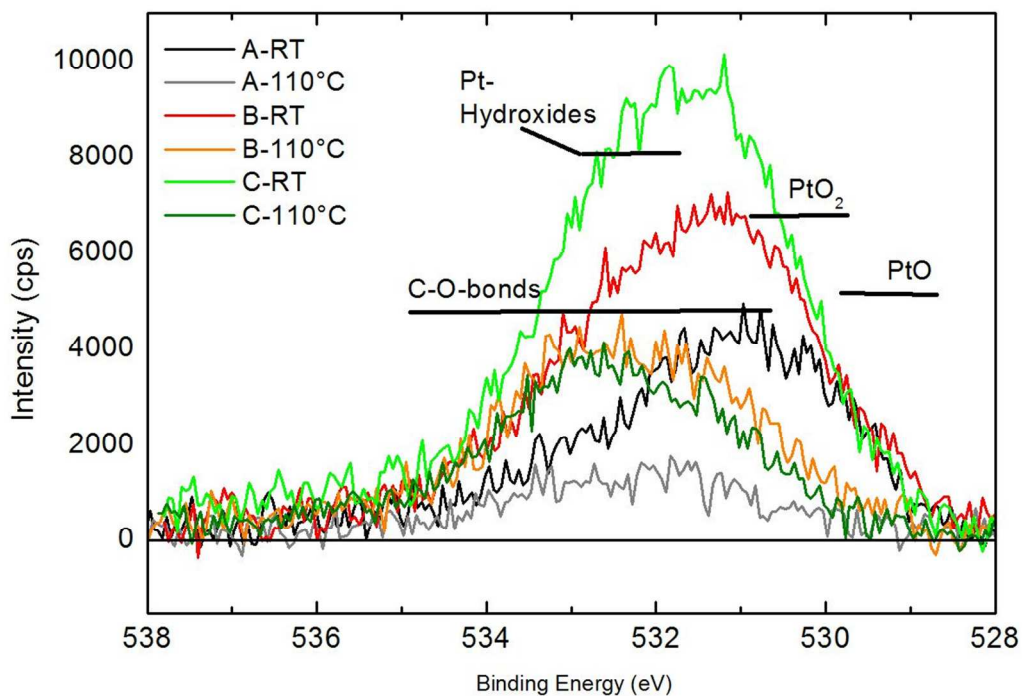
Figure S11: O 1s XPS spectrum of carbon A, B and C recorded before and after annealing at 110 °C. The energy regions that are characteristic for different contributions are indicated.

The observations made in the O1s XPS are reflected by the C1s spectra. Compared to carbon A, the carbons B and C are highly oxidized, as follows from the high contribution due to C-O bonds. Both show the whole set of functional group related peaks. As mentioned in the discussion of the O 1s spectrum, the quantity of C-O groups in carbon B and C does not change upon annealing at 110 °C. This is indicative for strongly bonded carboxyl/hydroxyl groups. Their higher abundance in carbon C is in agreement with the TG data (fig. S6 and fig. S7).
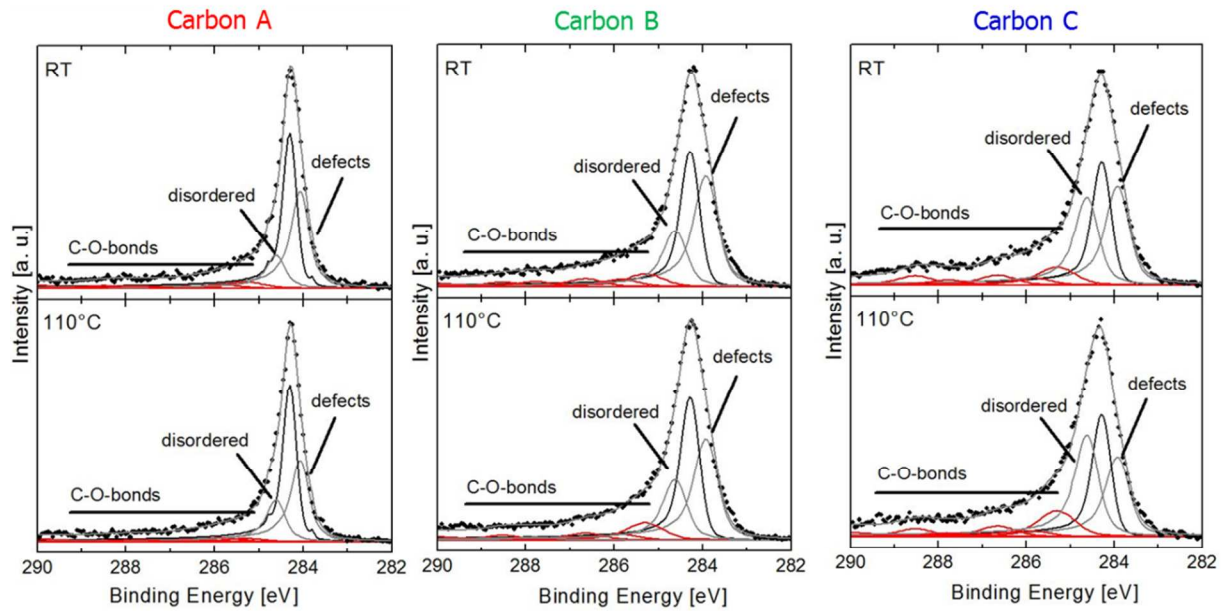
Figure S12 : C 1s XPS spectrum of carbon A, B and C recorded at RT and during annealing at 110 °C. Different contributions to the total intensity are indicated.

Additional information about the surface state of the carbons is provided by the C1s fits. Carbon C is quite disordered and, in accordance with XRD, Raman, EELS, HRTEM and TG, contains defective graphitic carbon. Carbon B is less disordered but still contains disordered carbon besides a very defective graphitic carbon. Carbon A has almost no disordered carbon, but shows, besides the graphitic peak, also intensity due to defects in graphitic carbon. In general, the surface defectiveness of carbon A is closer to the one in B, but A contains much less oxygen and a smaller portion of disordered carbon.

Table S3. Elemental analysis of the samples at room temperature using XPS and XRF techniques

XPS elemental analysis of Pt/carbon				XRF analysis of Pt/carbon		
	$Pt_{at\%}$	$C_{at\%}$	$O_{at\%}$		$Pt_{at\%}$	$C_{at\%}$
Pt/A T_{room}	1	80.2	18.8	Pt/A T_{room}	2.04	97.96
Pt/B T_{room}	0.4	85.1	14.5	Pt/B T_{room}	2.1	97.9
Pt/C T_{room}	0.35	79.2	20.4	Pt/C T_{room}	2.13	97.87

Table S4. Textural properties of carbon A, B and C.

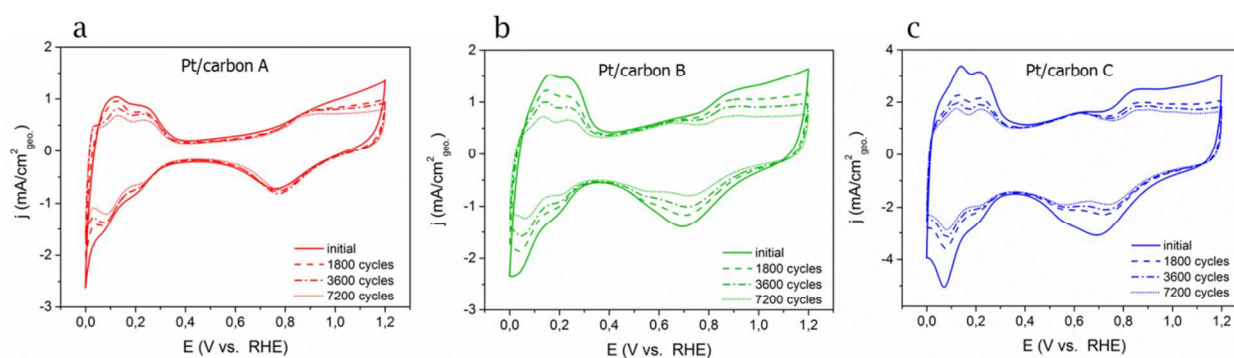| Sample	$S_{BET}\ [m^2g^{-1}]$	$V_{Total}\ [m^3g^{-1}]$	$V_{\mu icropore}\ [m^3g^{-1}]$	$S_{\mu icropore}\ [m^2g^{-1}]$
Carbon A	83	0.61	0.003	9
Pt/carbon A	75			
Carbon B	247	1.67	0.04	78
Pt/carbon B	155			
Carbon C	582	0.99	0.09	175
Pt/carbon C	362			

Figure S13. CV profiles recorded in N_2 saturated 0.1M $HClO_4$ aqueous solution at 50 mV/s
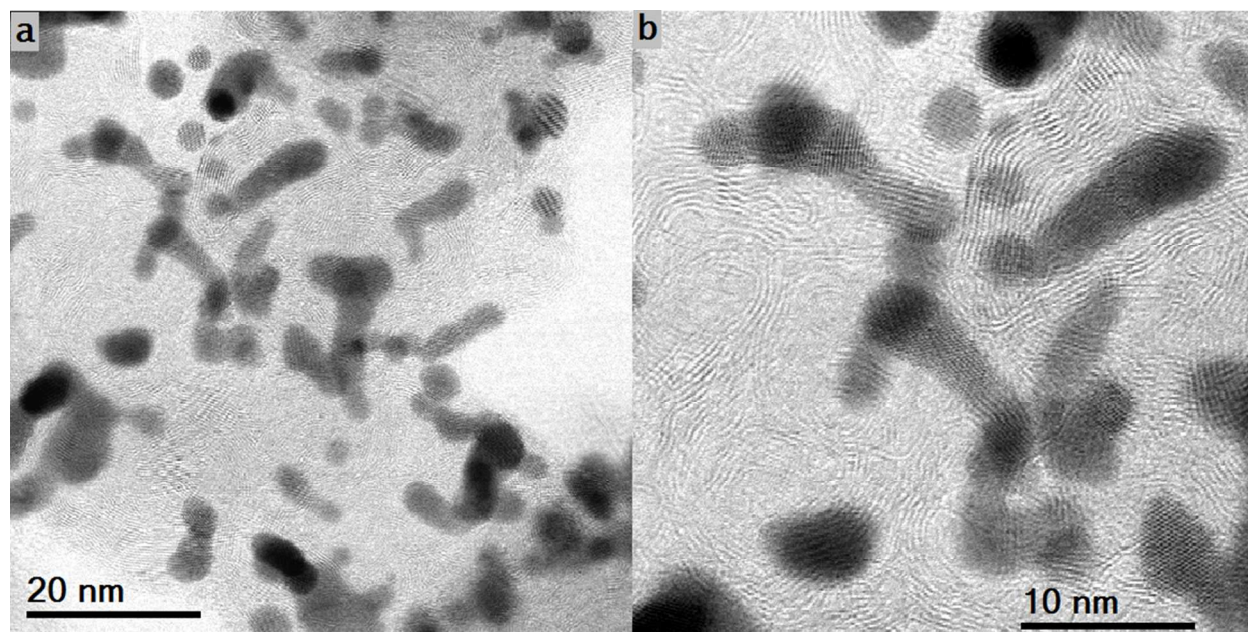
Figure S14. Bright-field STEM images show that Pt particles on carbon A preserve their elongated high-aspect ratio shape which is an indicator of the preserved good wetting after CV corrosion.
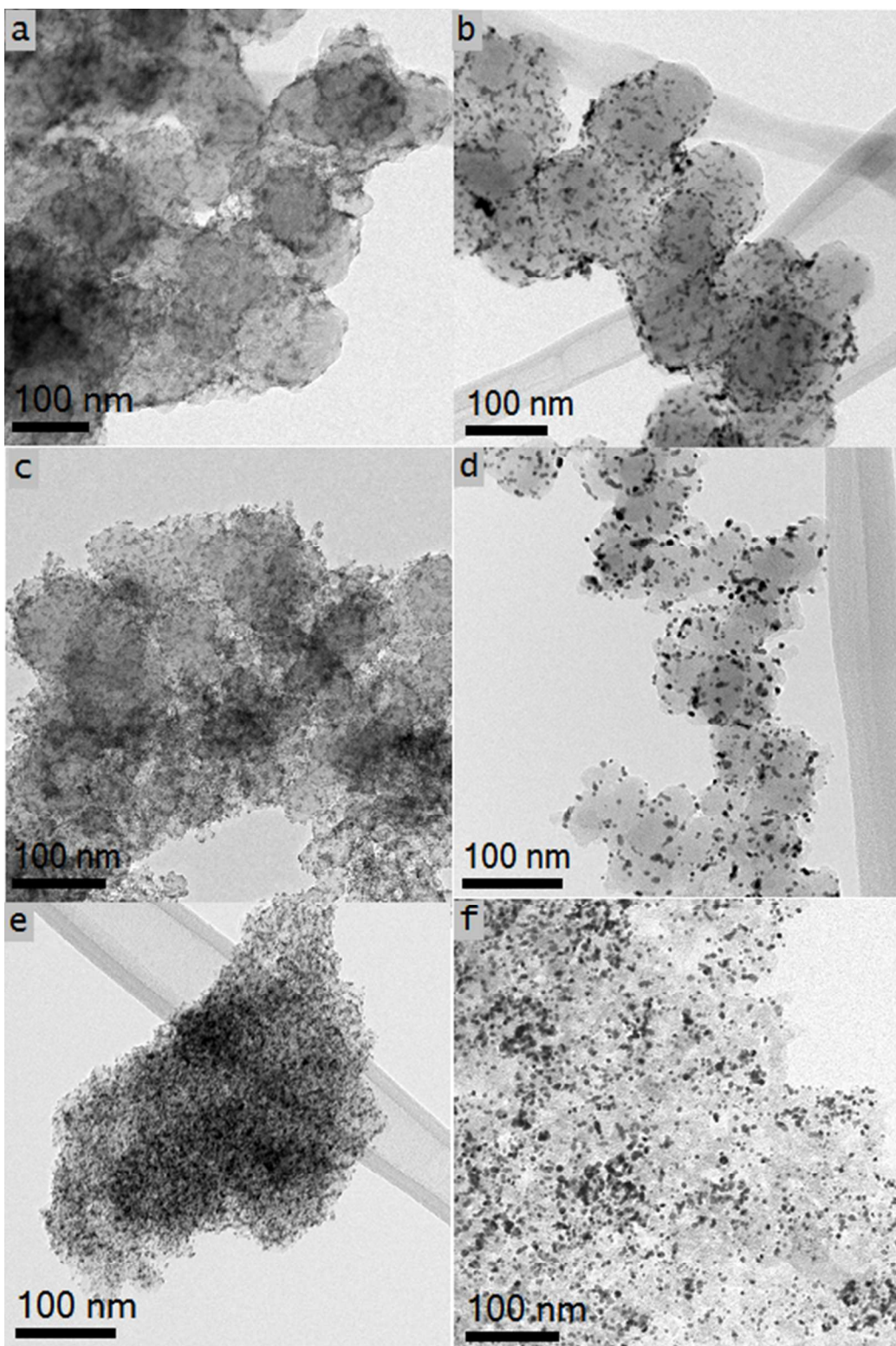
Figure S15. TEM overview images before and after CV corrosion. (a, b) the Pt/carbon A; (c, d) the Pt/carbon B; (e, f) the Pt/carbon C, respectively.
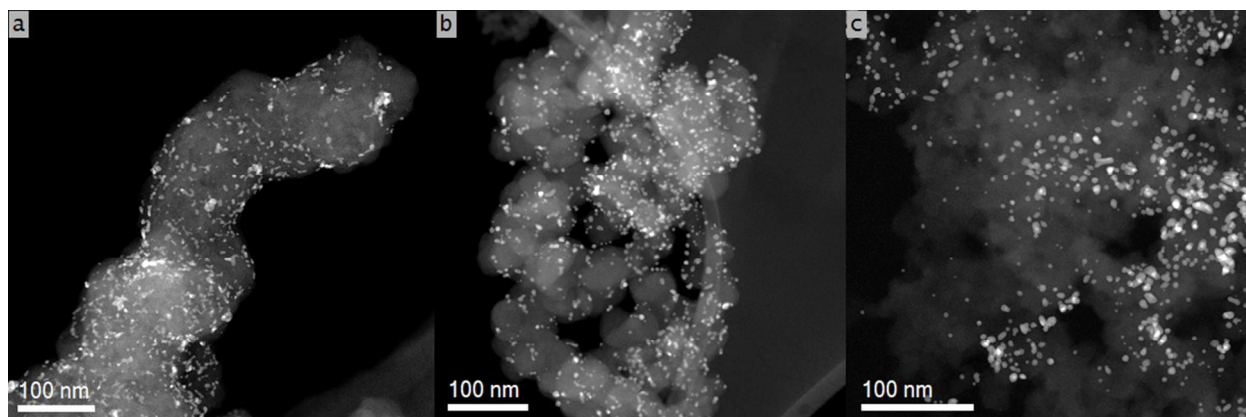
Figure S16. HAADF overview images after CV: (a-c) the Pt/carbon A, Pt/carbon B and Pt/carbon C, respectively.
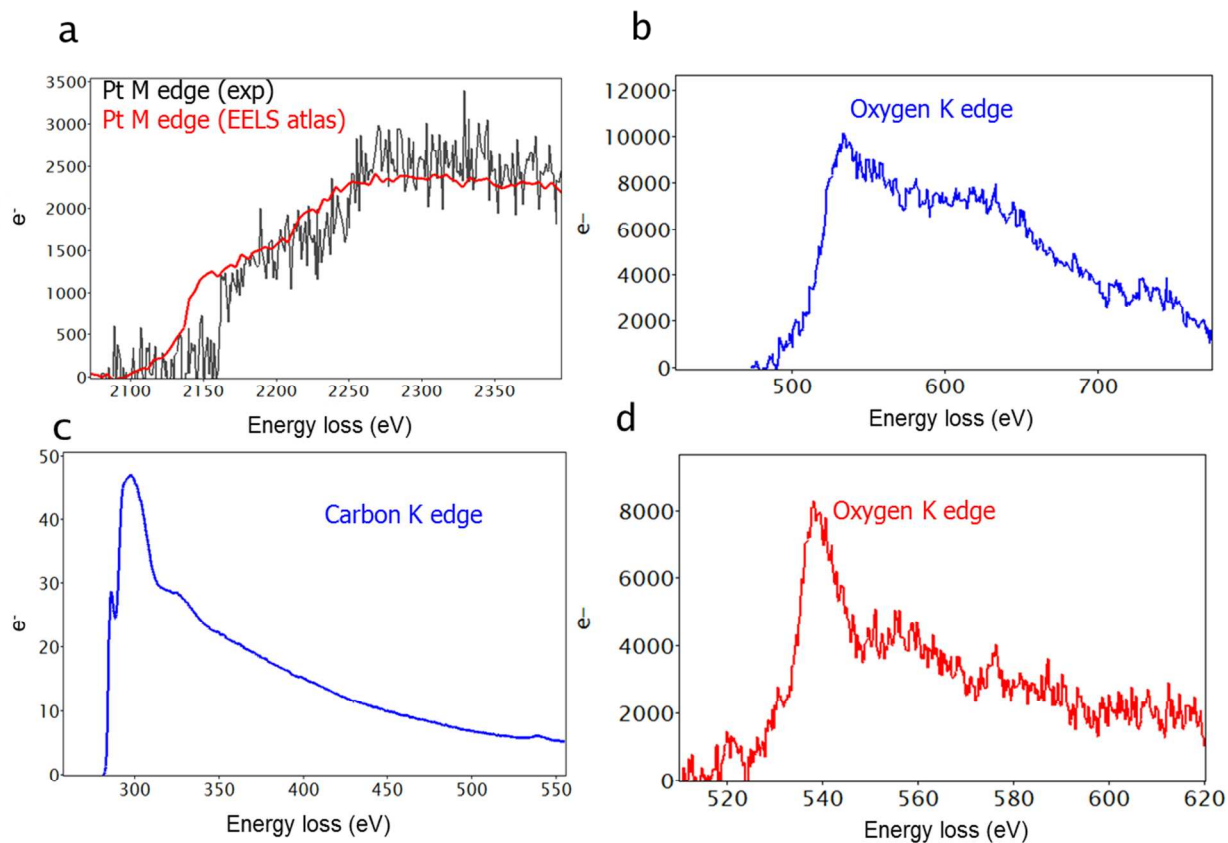

Figure S17. EELS spectra of corresponding EELS line scan of Pt/carbon A and Pt/carbon C samples after CA test: (a, b) the Pt/carbon A EELS spectra of Pt M-edge and O k-edge, respectively; (c, d) the Pt/carbon C EELS spectra of C K-edge and O k-edge, respectively.
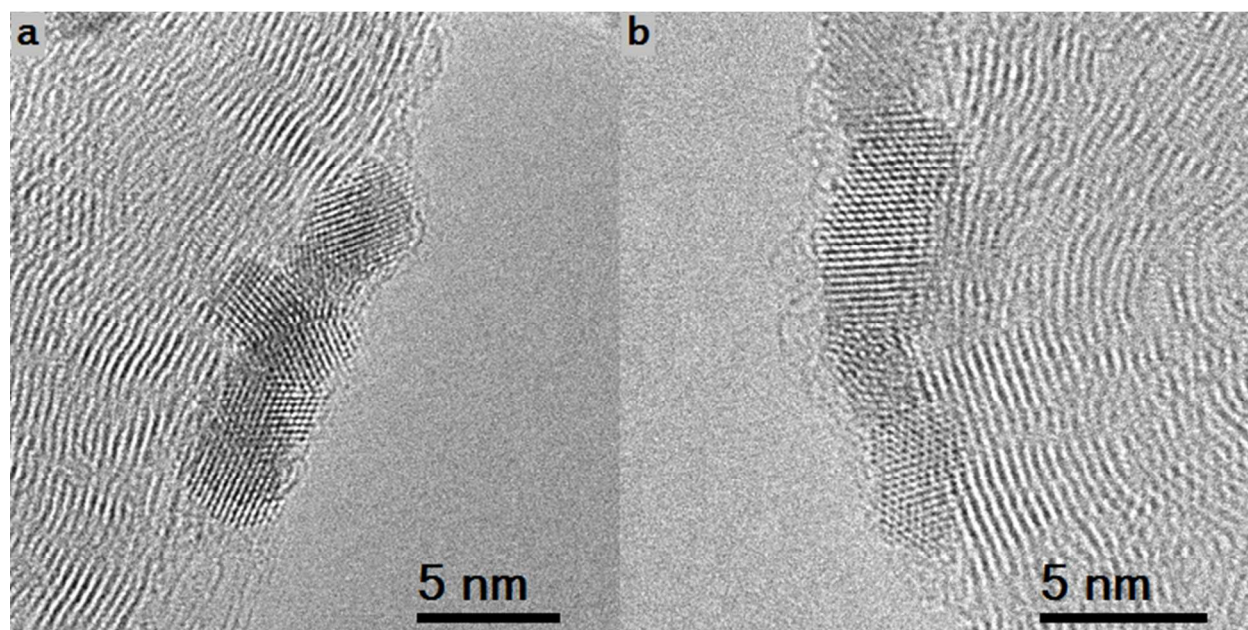
.

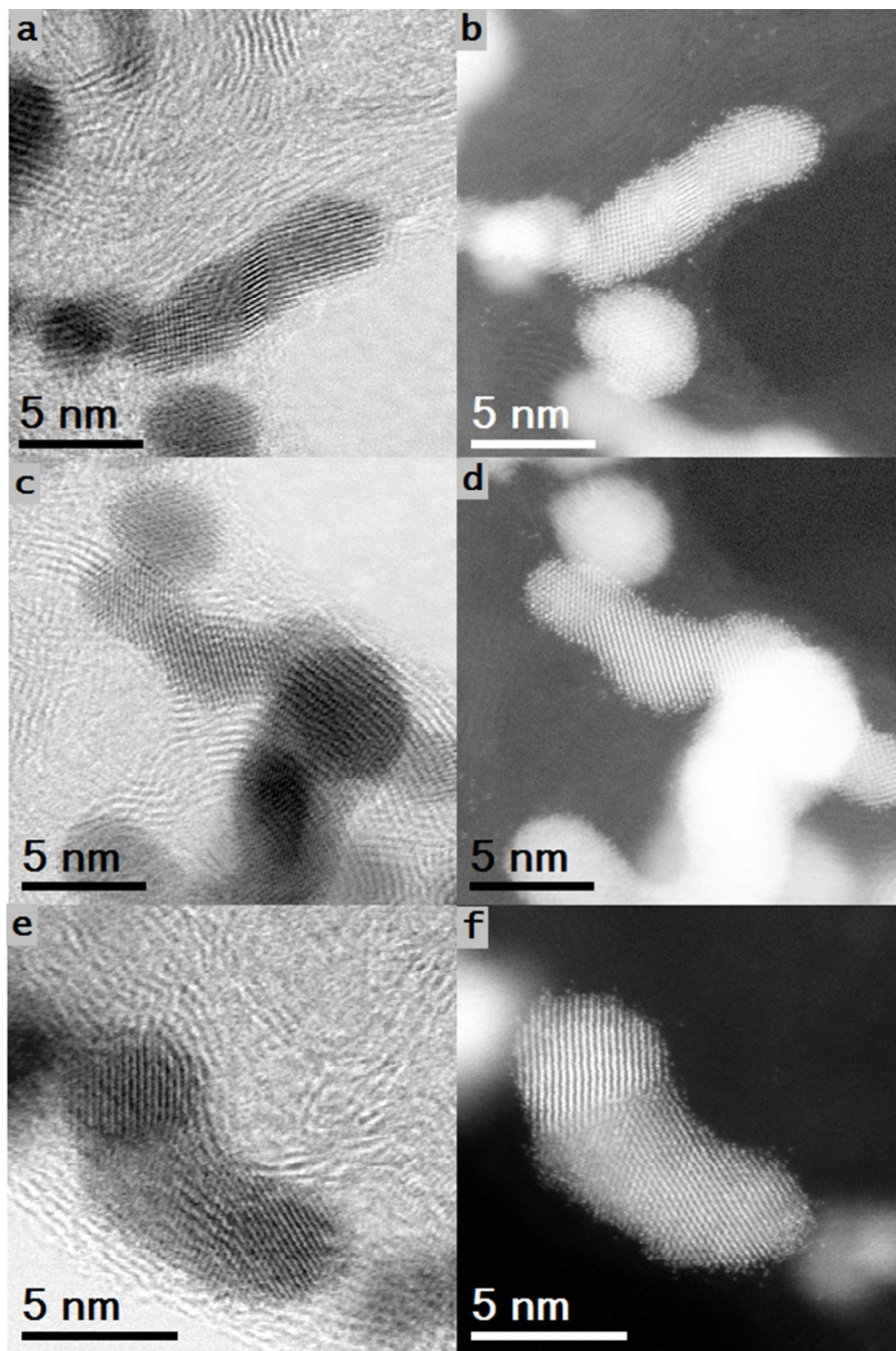Figure S 18. HRTEM images of the initial Pt/ carbon A show a good wetting of Pt rafts on the carbon support.

Figure S19. High-resolution STEM images of the Pt/carbon A sample (a, c, e-bright-field and b, d, f –HAADF images, respectively). Bright-field STEM images show how Pt rafts repeat the curvature of the carbon layers indicating a preserved strong Pt-carbon interaction after CV corrosion.

References

1. Yaovi Holade, Claudia Morais, Karine Servat, Teko W. Napporn and K. Boniface Kokoh *Phys. Chem. Chem. Phys*. **2014**, *16*, 25609.
2. Luis Castanheira, Wanderson O. Silva, Fabio H.B. Lima, Alexandre Crisci, Laetitia Dubau and Frédéric Maillard, *ACS Catal. 2015*, *5*, 2184−2194.